Research Article Vol. 60, No. 5 / 10 February 2021 / Applied Optics 1387

applied optics

Two-step calibration method for extrinsic parameters of an airborne camera

Dongming Yuan,[1,2,3] Yalin Ding,[1] Guoqin Yuan,[1,*] Feng Li,[1] Jian Zhang,[1] Yuanchao Wang,[1,2] and Lei Zhang[1]

[1]Changchun Institute of Optics, Fine Mechanics and Physics, Chinese Academy of Sciences, Changchun, Jilin 130033, China
[2]University of the Chinese Academy of Sciences, Beijing 100049, China
[3]Chinese Academy of Sciences, Key Laboratory of Airborne Optical Imaging and Measurement, Changchun, Jilin 130033, China
*Corresponding author: yuanguoqin@139.com

Received 12 October 2020; revised 21 December 2020; accepted 5 January 2021; posted 7 January 2021 (Doc. ID 412305); published 9 February 2021

In order to meet the accuracy requirements of target geo-location of a wide-area reconnaissance camera, it is necessary to calibrate the extrinsic parameters of the camera. A novel calibration method is proposed for the orientation relationship between the camera coordinate system (CCS) and the frame coordinate system (FCS). First, the calibration between the roll axis of the FCS and the CCS is carried out based on the method of the extended Kalman filter. Second, the calibration between the pitch axis of the FCS and the CCS is deduced based on the least mean square combined with the particle swarm optimization method. Then, the calibration accuracy of the proposed method is quantitatively analyzed by numerical simulation. Finally, a calibration experiment is conducted on verifying the effectiveness of the method.

https://doi.org/10.1364/AO.412305

1. INTRODUCTION

Airborne wide-area reconnaissance cameras are widely used in remote sensing and telemetry area due to their long operating distance and high imaging resolution [1]. With the improvement of customer's requirements, high-precision target geo-location has become an indispensable function of airborne cameras [2,3]. Many references have verified that the orientation error among the camera coordinate system (CCS), the frame coordinate system (FCS) and the position and orientation system (POS) coordinate system (PCS) is one of the main causes of target geo-location error [3–5]. Thus, after the optical-mechanical adjustment of an airborne camera, the calibration of the orientation relationship between the CCS, the FCS, and the PCS is required to achieve high-precision target geo-location.

Many researchers applied the calibration methods on visual inertial navigation or measurement systems, which can be classified as direct calibration methods and indirect calibration methods [6]. Azuma *et al.* [7] and Bajura *et al.* [8] proposed a direct calibration method based on geometric constraints and bore-sight technology for augmented reality systems. However, the application of the direct calibration method is limited due to the device design. Thus, the indirect methods are widely applied on the calibration of the orientation relationship in engineer practice. The indirect methods are mainly based on the camera pinhole imaging principle [9] and the mathematical model of inertial device measurement [10,11], by which the observation equations are established and solved. You *et al.* [12] adopted an inertial sensor to measure the angular velocity in the inertial measurement unit (IMU) coordinate system, and a camera to obtain the moving speed of the object's feature points on the image plane. Then the conversion relationship between the related coordinate systems could be obtained based on the above two velocities. Lobo and Dias [13,14] jointly proposed a calibration method in which the vertical direction is taken as the reference direction. The IMU was used to measure the acceleration of a force-balanced carrier. On the one hand, when the acceleration value measured by the IMU is equal to the gravity acceleration in a certain direction, the direction is considered as the vertical direction. On the other hand, the vertical direction was obtained by observing the vanishing point on a vertical side. Finally, the conversion relationship between the related systems is obtained by Horn's method [15]. Wang *et al.* [16] used a total station as a reference and deduced the relationship between the camera coordinate system and the total station coordinate system through a homograph. Then, combining with the measurement results of the IMU, the conversion relationship between the camera coordinate system and the IMU coordinate system could be obtained. Hol *et al.* [17] adopted extended Kalman filter (EKF) algorithm to estimate the extrinsic parameters of a camera and an IMU. The equations of the method were established based on the geometrical constraints in the object space and the regular movement of the platform. Its experiments indicated that the proposed algorithm is efficient. Ouyang *et al.* [18] used a similar approach to [17], the difference

of [18] is the corner detection on the geometrical constraints, in which linear constraint refinement and IMU-aided checkerboard corner modification were introduced to improve the calibration accuracy. Xu *et al.* [19] proposed a method which is based on the least mean square (LMS) algorithm to calibrate the orientation and translation relationship of an inertial and visual sensor. The method is simple and easy to be implemented, but the calibration accuracy is slightly low limited by the LMS. Gaurav *et al.* [20] adopted the Levenberg Marquardt algorithm to calibrate the extrinsic parameters between a 3D laser scanner and an omnidirectional camera. The calibration procedure required a planar checkerboard to be observed simultaneously by the laser scanner and the camera system from three views. The normal of the planar surface and 3D points lying on one surface provide constraints to form a non-linear optimization problem. Similarly, Aliakbarpour *et al.* [21] used an IMU to measure a freely moving bright spot instead of a checkerboard to decrease the number of points needed to a robust calibration. Fang *et al.* [22] and Dong *et al.* [23] established the observation equations based on the measurement on a checkerboard by a laser range finder and a camera. In particular, the checkerboard in [23] is V-shaped and it can improve the calibration accuracy. Yin *et al.* [24] adopted the Levenberg Marquardt algorithm to calibrate the extrinsic parameters of a multi-camera system of which the difficulty is that there is non-overlapping of the field of view (FOV). Both Deng *et al.* [25] and Arbabmir *et al.* [6] used the particle swarm optimization (PSO) algorithm to calibrate the extrinsic parameters of a visual-inertial navigation system. The novelty of [6] is that the PSO algorithm is combined with the genetic algorithm (GA) to prevent the iteration from premature convergence to local solution.

It can be found that the indirect calibration methods are mainly applied on current state-of-the-arts. They establish a unique calibration method according to the own characteristics of their research objects and adopt mature algorithms or improved algorithms to complete the calibration. However, it is not difficult to find that the mass and the volume of the research objects is relatively small, the focal length of the camera is short, and the FOV is large, which can make the device move according to a certain law to observe the indoor target, i.e., checkerboard, easily. The research object of this paper is a certain type of airborne camera with large volume, long focal length, and small FOV, which induce difficulties to calibrate its extrinsic parameters according to the methods in the current arts. In addition, the calibrated objects of current state-of-the-arts, such as an IMU and a camera, are rigidly connected together and installed on the motion platform or frame simultaneously. They can measure under the same motion, which could make full use of the complementary nature of each other device to improve the calibration accuracy as mentioned in [18]. In contrast to our research object, the IMU of the POS and the optical camera are installed in the fixed and rotating parts of the frame structure, respectively. Thus, the extrinsic parameters of the POS and frame, camera and frame need to be calibrated separately.

In this work, we propose a novel two-step calibration method for the extrinsic parameters between a camera and its frame of an airborne camera. The method can well adapt to the characteristics of this camera to complete its calibration. The actual operation is simple and feasible. Meanwhile, we have improved the matured algorithm used in each step to reduce the actual workload and improve the calibration accuracy. Specifically, our innovations of this paper are as follows:

(a) A novel two-step calibration method is proposed to calibrate the extrinsic parameters between the FCS and the CCS of an airborne camera. In the method, the camera is rotated around its roll axis and pitch axis respectively to image a star point passing through a collimator. The calibration parameters are obtained by analyzing the relation between the trajectory of the image point and the corresponding position of each axis. The mathematical model of the calibration method is established.

(b) In the first step of the calibration, the EKF algorithm used in this paper differs from the traditional in that during the iteration process, when the states indicate that it has rotated one circle around the roll axis, the measure points in the original circle will be reused to complete the entire iteration. That is, the real experiment only needs to measure about 60 points in a circle, which remarkably reduces the workload.

(c) In the second step of the calibration, a two-step optimization algorithm, i.e., LMS-PSO, is proposed, which could reduce the error caused by linearization and ensure that the global optimal solution can be obtained. First, an approximate estimate of the optimal solution is obtained by the LMS algorithm. Second, the initial population of the PSO algorithm is generated based on this approximation, which can obtain more accurate result. In addition, a mutation link is introduced into the iteration of PSO, which can ensure the optimization result will not deviate too much from the approximation to guarantee the correctness.

Considering the conflicts of interest issues, only the calibration method of the CCS and the FCS will be included in this paper. However, the calibration work of the PCS and the FCS could be carried out separately which would not have an impact on the completeness of this article. For the above content, the remaining full text is arranged as follows: the calibration method is introduced in Section 2; the numerical simulation is presented in Section 3 while the experiment is depicted in Section 4; finally, the conclusion of this paper is given in Section 5.

2. CALIBRATION METHOD

A. Problem Statement

As a general kind of aerial photograph equipment, the airborne wide-area reconnaissance camera can achieve high-precision target geo-location. As shown in Fig. 1, the camera studied in this paper is mainly composed of a frame system, an optical imaging system, and a servo control system:

(a) The frame system consists of fixed and rotating structural parts, in which the base is fixed and the roll and pitch rotary shaft systems are rotating. In the next content, the roll rotary shaft system is equivalent to the roll axis, while the pitch rotary shaft system is equivalent to the pitch axis. In working condition, the camera rotates around its roll axis

to increase the accommodation width in the vertical direction of flight. In the same way, the camera rotates around its pitch axis to increase the accommodation width in the flight direction. The FCS is set on the two rotary shaft systems of the frame system. Specifically, it is denoted as $o_F x_F y_F z_F$ with its original point located at the intersection of the roll axis and the pitch axis. The X axis lies along the roll axis and points to the head of the base. The Y axis lies along the pitch axis and points to the right (looking from the rear to the head). The Z axis form an orthogonal right-handed (RH) set. This coordinate system rotates with the roll/pitch axis.

(b) The optical imaging system consists of an optical lens and a detector. The CCS is set on the optical imaging system. Specifically, it is denoted as $o_C x_C y_C z_C$ with its original point located at the optical principalpoint of the camera. The X axis lies along the line-of-sight (LOS) and points to the head of the base. The Y axis, which is perpendicular to its X axis, lies along the pitch axis and points to the right in the ideal case. The Z axis completes the RH orthogonal set. This coordinate system rotates with the roll/pitch axis.

(c) The POS system belongs to the servo control system, which is composed of a global position system (GPS) antenna located at an open space on the aircraft, and an IMU device installed at the rear of the frame base. The PCS is set on the POS system and denoted as $o_P x_P y_P z_P$. In the ideal case the match between the positioning surfaces of the POS system and the corresponding positioning surfaces of the frame base is perfect and the two rotary shaft systems are at zero position. The X axis of the PCS lies along the roll axis and points to the head of the base. The Y axis lies along the pitch axis and points to the right (looking from the rear to the head). The Z axis form an orthogonal RH set. This coordinate system does not rotate with the roll/pitch axis.

Ideally, the CCS ($o_C x_C y_C z_C$) and PCS ($o_P x_P y_P z_P$) are consistent with the frame coordinate system. However, due to manufacture errors of optical and mechanical parts and assembly errors of each group, the angle and position error between the three coordinate systems is inevitable. As a result, the calibration of extrinsic parameters among the CCS, FCS, and PCS is necessary for improving the target location accuracy. It should be noted that the positional relationship of the three coordinate systems has little influence on target geo-location accuracy and could be ignored [26,27]; therefore, the relationship is not within the scope of this paper.

Specifically, the angle errors between the FCS and the CCS are α_{FC}, β_{FC}, and θ_{FC}, as shown in Fig. 2. In terms of the above angle errors, a two-step calibration method is described in this paper. In the first step, the relationship between the roll axis of the FCS and the CCS is calibrated (α_{FC}, β_{FC}). In the second step, the relationship between the pitch axis of the FCS and the CCS is calibrated (θ_{FC}).

B. Calibration of the Roll Axis of the FCS and the CCS

According to the mechanical structure of the airborne camera, the pitch axis of the FCS is mounted on the roll axis of the FCS. It must be expressed by an Euler angle with the roll axis and an Euler angle with the pitch axis subsequently when the airborne camera rolls around with its two axes. Based on this, the whole calibration work can be divided into two steps and the relationship between the roll axis of the FCS and the CCS is first calibrated here. Because the pitch axis of the FCS will not be used in the first step, the scan head should be removed at the beginning of this step. Then the optical system is rotated around the roll axis of the FCS to image a star point passing through a collimator at different roll angles. The constraint equations can be established considering the relationship among the roll angles, the image point coordinates, and the parameters to be calibrated. The specific calibration principle is shown in Fig. 3.

In Fig. 3, $o_C x_C y_C z_C$ is the coordinate of the airborne camera, $o_F x_F y_F z_F$ is the coordinate of the frame, which is consistent

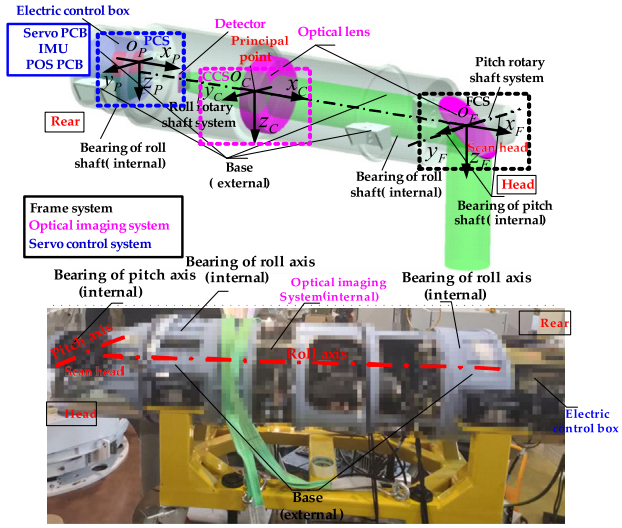

Fig. 1. System model of this paper.

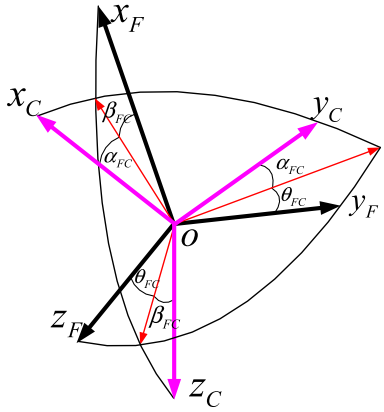

Fig. 2. Angle errors between the FCS and CCS.

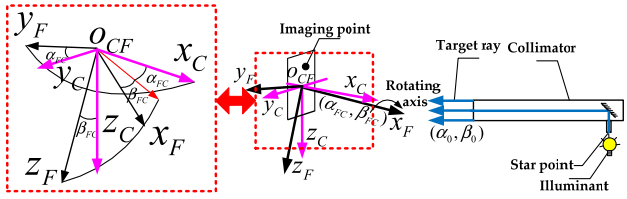

Fig. 3. Calibration principle of the roll axis and CCS.

with the relationship depicted in Fig. 1. $(\alpha_{FC}, \beta_{FC})$ are the Euler angles of the roll axis vector of the FCS in the CCS. The rotation sequence of the roll axis in the CCS is the CCS rotates around $o_C z_C$ with the angle of α_{FC} first, and then rotates around $o_C y_C$ with the angle of β_{FC}. In this way, the $o_C x_C$ will coincide with the $o_F x_F$. These two angles are the calibration parameters of this step, which should be calibrated together to determine the roll axis vector in the CCS. In the same way, (α_0, β_0) are the two Euler angles of the target ray vector in the CCS. During this calibration step, the CCS rotates around $o_F x_F$ and images a star point passing through a collimator at different angles. The non-linear constraint equations can be established through studying the relationship among the roll angles, the image point coordinates, and the parameters $(\alpha_{FC}, \beta_{FC})$, (α_0, β_0). According to the pinhole camera model, we have

$$\mathbf{P_C} = \begin{vmatrix} P_x^C \\ P_y^C \\ P_z^C \end{vmatrix} = \mathbf{L_z}(-\alpha_0)\mathbf{L_y}(-\beta_0) \begin{vmatrix} 1 \\ 0 \\ 0 \end{vmatrix}, \tag{1}$$

$$\mathbf{p_C} = \begin{vmatrix} p_y^C \\ p_z^C \end{vmatrix} = \begin{vmatrix} 0 & -f/P_x^C & 0 \\ 0 & 0 & -f/P_x^C \end{vmatrix} \begin{vmatrix} P_x^C \\ P_y^C \\ P_z^C \end{vmatrix}, \tag{2}$$

where $\mathbf{L_y}(\beta) = \begin{vmatrix} \cos\beta & 0 & -\sin\beta \\ 0 & 1 & 0 \\ \sin\beta & 0 & \cos\beta \end{vmatrix}$, $\mathbf{L_z}(\alpha) = \begin{vmatrix} \cos\alpha & \sin\alpha & 0 \\ -\sin\alpha & \cos\alpha & 0 \\ 0 & 0 & 1 \end{vmatrix}$ are the rotation matrices; $\mathbf{P_C}$ is the target ray vector in the CCS; f is the focal length of the optical system; and $\mathbf{p_C}$ is the coordinate of the image point in the CCS. The focal length and the principal point coordinate could be obtained through Zhang's [28] or Yuan's [29] method.

While the CCS is fixed, the rotation angle $-\theta$ of the optical system around the roll axis is equivalent with the rotation angle θ of the target ray. Then the target ray vector in the CCS could be expressed as

$$\mathbf{P}_C(\theta) = \mathbf{R}(\theta)\mathbf{P}_C, \tag{3}$$

where $\mathbf{R}(\theta) = I + (\sin\theta)\mathbf{K} + (1-\cos\theta)\mathbf{K}^2$ is the Rodrigues' rotation formula. $\mathbf{K}$ is the skew-symmetric matrix which is defined as

$$\mathbf{K} = [\mathbf{k}\times] = \begin{vmatrix} 0 & -k_z & k_y \\ k_z & 0 & -k_x \\ -k_y & k_x & 0 \end{vmatrix}, \tag{4}$$

where $\mathbf{k} = (k_x, k_y, k_z)^T$ is the roll axis vector calculated by

$$\mathbf{k} = \begin{vmatrix} k_x \\ k_y \\ k_z \end{vmatrix} = \mathbf{L_z}(-\alpha_{FC})\mathbf{L_y}(-\beta_{FC}) \begin{vmatrix} 1 \\ 0 \\ 0 \end{vmatrix}. \tag{5}$$

Therefore, the target ray vector after rotation θ can be rewritten as

$$\begin{cases} P_x^C(\theta) = \cos\alpha_0\cos\beta_0[1-(1-\cos\theta)(\sin\alpha_{FC}^2\cos\beta_{FC}^2 \\ \quad + \sin\beta_{FC}^2)] + \sin\alpha_0\cos\beta_0[\sin\beta_{FC}\sin\theta \\ \quad + (1-\cos\theta)\cos\alpha_{FC}\sin\alpha_{FC}\cos\beta_{FC}^2] \\ \quad - \sin\beta_0[\sin\alpha_{FC}\cos\beta_{FC}\sin\theta \\ \quad - (1-\cos\theta)\cos\alpha_{FC}\cos\beta_{FC}\sin\beta_{FC}] \\ P_y^C(\theta) = \cos\alpha_0\cos\beta_0[-\sin\beta_{FC}\sin\theta \\ \quad + (1-\cos\theta)\cos\alpha_{FC}\sin\alpha_{FC}\cos\beta_{FC}^2] \\ \quad + \sin\alpha_0\cos\beta_0[1-(1-\cos\theta) \\ \quad \times(\cos\alpha_{FC}^2\cos\beta_{FC}^2 + \sin\beta_{FC}^2)] \\ \quad + \sin\beta_0[\cos\alpha_{FC}\cos\beta_{FC}\sin\theta \\ \quad + (1-\cos\theta)\sin\alpha_{FC}\cos\beta_{FC}\sin\beta_{FC}] \\ P_z^C(\theta) = -\cos\alpha_0\cos\beta_0[\sin\alpha_{FC}\cos\beta_{FC}\sin\theta \\ \quad + (1-\cos\theta)\cos\alpha_{FC}\cos\beta_{FC}\sin\beta_{FC}] \\ \quad + \sin\alpha_0\cos\beta_0[\cos\alpha_{FC}\cos\beta_{FC}\sin\theta \\ \quad - (1-\cos\theta)\sin\alpha_{FC}\cos\beta_{FC}\sin\beta_{FC}] \\ \quad - \sin\beta_0[1-(1-\cos\theta)\cos\beta_{FC}^2] \end{cases}. \tag{6}$$

Then the observation equations can be deduced by substituting Eq. (6) into Eq. (2):

$$\begin{cases} p_y^C = f_1(\alpha_0, \beta_0, \alpha_{FC}, \beta_{FC}, \theta) \\ p_z^C = f_2(\alpha_0, \beta_0, \alpha_{FC}, \beta_{FC}, \theta) \end{cases}, \tag{7}$$

where θ is the dynamic variable, and $(\alpha_0, \beta_0, \alpha_{FC}, \beta_{FC})$ is the variable vector to be solved. These non-linear equations will be solved through EKF in this paper in Section 3.

C. Calibration of the Pitch Axis of the FCS and the CCS

After calibrating the Euler angles $(\alpha_{FC}, \beta_{FC})$ of the roll axis, there is one Euler angle θ_{FC} of rotation around $o_F x_F$ left to set up the relationship between the FCS and the CCS. It needs to be explained here that although $(\alpha_{FC}, \beta_{FC})$ are both quite minimal where $o_F x_F$ almost coincides with $o_C x_C$. Therefore, the Euler angle of rotation around $o_F x_F$ is approximately equal to the angle of rotation around $o_C x_C$ regardless of its value.

The calibration principle of the Euler angle θ_{FC} in this paper is shown in Fig. 4. As can be seen from Fig. 4, the actual FCS is obtained by rotating the CCS around its X axis with the angle θ_{FC}. By rotating the scanning mirror around the pitch axis, the star point coming from a collimator can be observed. Then the θ_{FC} can be obtained through studying the trajectory of the above image points. According to Fig. 3, the optical system rotates a certain angle around the roll axis to image the target point, and its mathematical model can be expressed as follows:

$$\mathbf{p'_C} = \begin{vmatrix} 0 \\ p'_{Cy} \\ p'_{Cz} \end{vmatrix} = \mathbf{T}\left[\mathbf{L_x}^{-1}(\theta_{FC})\mathbf{M}\mathbf{L_x}(\theta_{FC})\mathbf{L_x}(\delta) \begin{vmatrix} x_0 \\ y_0 \\ H \end{vmatrix} + \begin{vmatrix} L_1 \\ 0 \\ 0 \end{vmatrix}\right] + \begin{vmatrix} f \\ 0 \\ 0 \end{vmatrix}, \tag{8}$$

where $(x_0, y_0, H)^T$ is the object coordinate in an ideal FCS when the roll angle equals to zero; the rotation matrix of x axis $\mathbf{L_x}(\cdot)$ can be expressed as

$$\mathbf{L_x}(\cdot)=\begin{vmatrix}1 & 0 & 0\\ 0 & \cos(\cdot) & \sin(\cdot)\\ 0 & -\sin(\cdot) & \cos(\cdot)\end{vmatrix}, \tag{9}$$

where δ is the roll angle of the optical system; θ_{FC} is the Euler angle to be calibrated; $\mathbf{M}$ can be expressed as [30,31]

$$\mathbf{M}=\mathbf{I}-2\mathbf{N}\mathbf{N}^{\mathbf{T}}, \tag{10}$$

where $\mathbf{N}=(\cos\gamma,\ 0,\ -\sin\gamma)^T$; γ is the angle between the normal of the scanning mirror and the optical axis; and $\mathbf{I}$ is the identity matrix, then $\mathbf{T}$ can be expressed as

$$\mathbf{T}=\frac{f}{f+x_0\cos 2\gamma-\sin 2\gamma[H\cos(\delta+\theta_{FC})-y_0\sin(\delta+\theta_{FC})]-L_1}\mathbf{I}, \tag{11}$$

where L_1 is the distance between the intersection of the scanning mirror and the optical axis and the principal point. Then, by substituting Eqs. (9)–(11) into Eq. (8), $\mathbf{p}'_{\mathbf{C}}$ can be obtained:

$$\mathbf{p}'_{\mathbf{C}}=\begin{vmatrix}0\\ p'_{Cy}\\ p'_{Cz}\end{vmatrix}=\frac{f}{f+x_0\cos 2\gamma-H_1\sin 2\gamma-L_1}\mathbf{L_x}(-\theta_{FC})\times\begin{vmatrix}0\\ B\\ x_0\sin 2\gamma+H_1\cos 2\gamma\end{vmatrix}, \tag{12}$$

where H_1 and B can be denoted respectively as

$$H_1=H\cos(\delta+\theta_{FC})-y_0\sin(\delta+\theta_{FC}), \tag{13}$$

$$B=y_0\cos(\delta+\theta_{FC})+H\sin(\delta+\theta_{FC}). \tag{14}$$

An auxiliary camera coordinate system (ACCS) can be introduced. The ACCS can be transformed by rotating the CCS around its X axis with θ_{FC} and denoted as $o'_Cx'_Cy'_Cz'_C$. Then $\mathbf{p}'_{\mathbf{C}}$ of Eq. (12) can be expressed in the ACCS as

$$\mathbf{p}''_{\mathbf{C}}=\begin{vmatrix}0\\ p''_{Cy}\\ p''_{Cz}\end{vmatrix}=\frac{f}{f+x_0\cos 2\gamma-H_1\sin 2\gamma-L_1}\times\begin{vmatrix}0\\ B\\ x_0\sin 2\gamma+H_1\cos 2\gamma\end{vmatrix}. \tag{15}$$

Through rigidly deriving, the coordinate value $(p''_{Cy},\ p''_{Cz})$ satisfies the condition

$$\frac{\left[p''_{Cy}+\frac{fB(f-L_1)}{H_1^2+x_0^2-(f-L_1)^2}\right]^2}{\frac{f^2B^2(H_1^2+x_0^2)}{[H_1^2+x_0^2-(f-L_1)^2]^2}}-\frac{(p''_{Cz})^2}{\frac{f^2(H_1^2+x_0^2)}{H_1^2+x_0^2-(f-L_1)^2}}=1. \tag{16}$$

It can be concluded from Eq. (16) that the trajectory of the image point in the ACCS is a hyperbola, where the symmetry axis of the hyperbola $o'_Cy'_C$ will pass through the two focuses. And the angle between $o'_Cy'_C$ and o_Cy_C is the Euler angle to be calibrated, i.e., θ_{FC}.

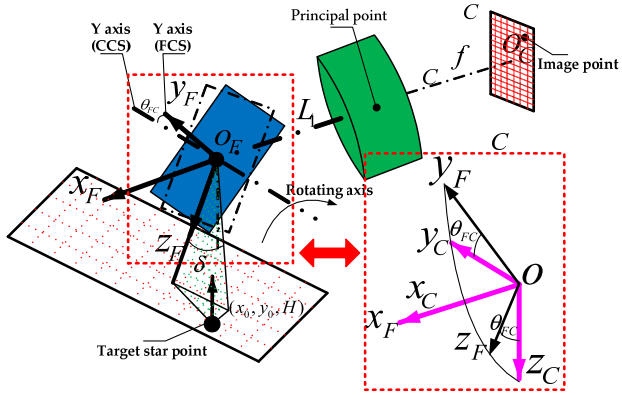

Fig. 4. Calibration principle of θ_{FC}.

3. NUMERICAL SIMULATION

A. Simulation for the Calibration of the Roll Axis of the FCS and the CCS

The calibration method of the roll axis of the FCS and the CCS is simulated based on the EKF in this section. $(\alpha_0,\ \beta_0,\ \alpha_{FC},\ \beta_{FC})$ is the state variable vector, and the EKF model can be expressed as

$$\begin{cases}\mathbf{S}^k=\mathbf{I}\mathbf{S}^{k-1}+\mathbf{s}^k\\ \mathbf{p}_C^k=\mathbf{f}(\mathbf{S}^k)+\mathbf{m}^k\end{cases}, \tag{17}$$

where $\mathbf{S}^k=(\alpha_0,\ \beta_0,\ \alpha_{FC},\ \beta_{FC})^T$ is the state variable vector of step k; $\mathbf{I}$ is the identity matrix; $\mathbf{s}^k$ is the process noise of step k; $\mathbf{p}_C^k$ is the measure result of the image point coordinate of step k; $\mathbf{f}(\cdot)=(f_1(\cdot),\ f_2(\cdot))^T$, where $f_1(\cdot)$ and $f_2(\cdot)$ are seen in Eq. (7); and $\mathbf{m}^k$ is the measurement noise of the step k.

The dynamic variable of the above EKF model is θ in Eq. (7). MATLAB is utilized to simulate the calibration method with the simulation parameters shown in Table 1.

According to the parameters in Table 1, the numerical simulation is carried out by using the EKF method. The convergence process of the state variables and observation image points are shown in Fig. 5.

As can be seen from Fig. 5, when the number of iteration steps exceeds 1044, each error of the state variables is $\leq$0.00028°. It should be emphasized here that the measure points in one circle will be reused when the iteration step is greater than 60, to ensure the convergence accuracy and reduce the actual workload. In order to fully illustrate the convergence situation

Table 1. Simulation Parameters of Calibrating the Roll Axis of the FCS and CCS

Parameters		Value
Camera parameters	Size of pixel (m)	7.4×10^{-6}
	Focal length (m)	1.85
True value	State variable (°)	$(0.022,\ 0.031,\ 0.013,\ 0.015)^T$
Initial value	State variable (°)	$(0.056,\ 0.056,\ 0.056,\ 0.056)^T$
Noise	Noise of process ("·")	diag(100, 100, 100, 100)
	Noise of measure (pixel^2)	diag(1, 1)
Dynamic variable	Roll angle (°)	$(0,\ 6,\ 12,\ \ldots,\ 354)^T$

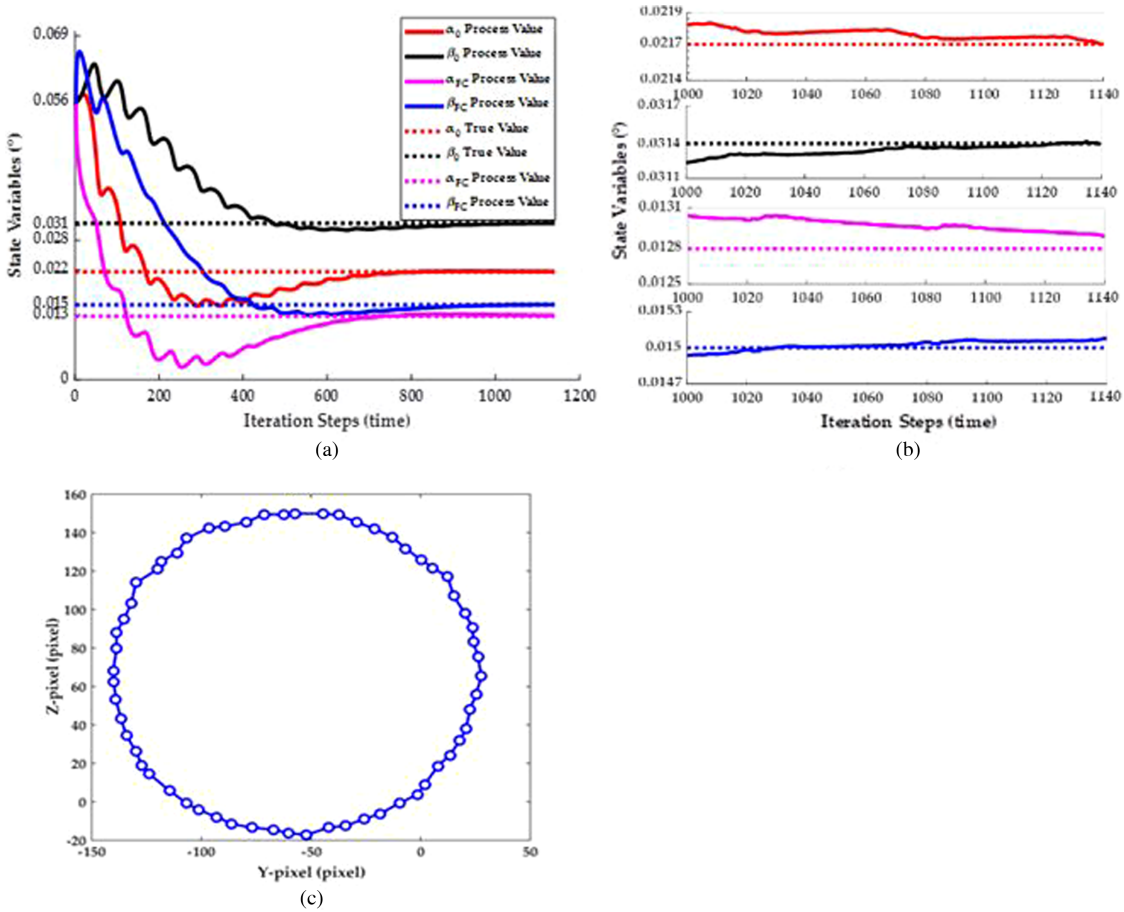

Fig. 5. Simulation results: (a) the convergence process of state variables; (b) the convergence process with maximum state variables error ≤0.00028°; (c) the measured image points of simulation.

and eliminate accidental factors, the above simulation process is repeated 10,000 times in this paper. The iteration step value is extracted when the maximum error of state variables is ≤0.00028° and its frequency distribution histogram is depicted in Fig. 6.

As can be seen from Fig. 6, the probability density distribution is a bi-modal function distribution, where the peak interval is either at [945, 950] or [990, 995] and the entire distribution interval is [890, 1133]. In order to ensure the actual calibration accuracy, the number of iteration steps is required to be above 1133 and 0.00028° (3σ) is treated as the calibration accuracy of the roll axis under this condition.

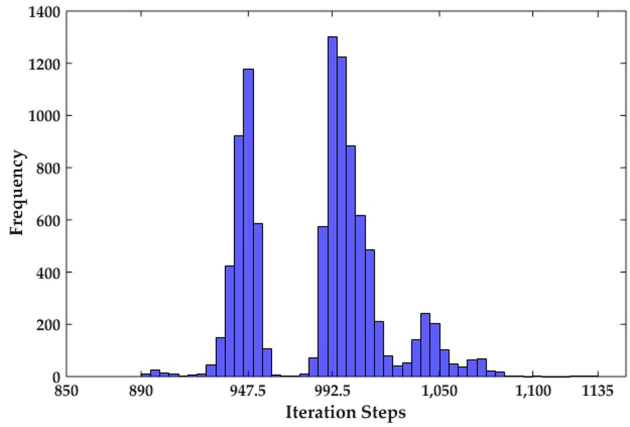

Fig. 6. Frequency distribution histogram of iteration step with 0.00028° accuracy.

B. Simulation for the Calibration of the Pitch Axis of the FCS and the CCS

The method to solve the Euler angle θ_{FC} is simulated in this section. And the general route of the method is to solve an initial value through an analytical method first and to refine the calibration parameters through an optimization algorithm second, which is inspired by [32]. According to the previous description, the calibration of θ_{FC} can be transformed into the calculation of the coordinates of the hyperbolic focuses. The coordinates of the two focuses are set as $F_1(y_{F1}, z_{F1})$ and $F_2(y_{F2}, z_{F2})$ under the condition of $y_{F1} > y_{F2}$. Then the hyperbolic equation can be denoted as

$$\sqrt{(y-y_{F2})^2+(z-z_{F2})^2}-\sqrt{(y-y_{F1})^2+(z-z_{F1})^2}=2a, \tag{18}$$

where (y, z) is the imaging point coordinate of the target and $(y_{F1}, z_{F1}, y_{F2}, z_{F2}, a)$ is the vector to be solved. The above formula is an implicit non-linear observation equation, which can be linearized through the Taylor expansion:

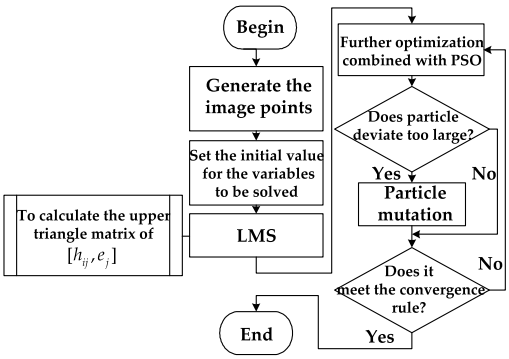

Fig. 7. Simulation process of θ_{FC}. It should be noted that the matrix $[h_{ij}, e_j]$ is ill-conditioned. Equation (21) cannot be solved through the Jacobian iterative method, Gaussian–Seidel iterative method, etc., when the LMS is adopted to solve the equations. We would adopt the upper triangle method to solve these equations in this paper.

$$\begin{aligned} E &= \sqrt{(y-y_{F2})^2+(z-z_{F2})^2} \\ &\quad -\sqrt{(y-y_{F1})^2+(z-z_{F1})^2}-2a \\ &\approx E^0+\frac{\partial E}{\partial y_{F1}}(y_{F1}-y_{F1}^0)+\frac{\partial E}{\partial z_{F_1}}(z_{F1}-z_{F1}^0) \\ &\quad +\frac{\partial E}{\partial y_{F2}}(y_{F2}-y_{F2}^0)+\frac{\partial E}{\partial z_{F2}}(z_{F2}-z_{F2}^0)+\frac{\partial E}{\partial a}(a-a^0) \\ &= E^0+\frac{\partial E}{\partial y_{F1}}\Delta y_{F1}+\frac{\partial E}{\partial z_{F1}}\Delta z_{F1} \\ &\quad +\frac{\partial E}{\partial y_{F2}}\Delta y_{F2}+\frac{\partial E}{\partial z_{F2}}\Delta z_{F2}+\frac{\partial E}{\partial a}\Delta a \approx 0, \end{aligned} \tag{19}$$

where

$$E^0=\sqrt{(y-y_{F2}^0)^2+(z-z_{F2}^0)^2} -\sqrt{(y-y_{F1}^0)^2+(z-z_{F1}^0)^2}-2a^0, \tag{20}$$

$(y_{F1}^0, z_{F1}^0, y_{F2}^0, z_{F2}^0, a^0)$ is the initial value, and $\frac{\partial E}{\partial \cdot}$ is the function value of the corresponding partial derivative at the initial value and observation value. n is set as the total number of the observation, then it can be deduced:

$$\begin{vmatrix} h_{11} & \cdots & h_{51} \\ \vdots & \vdots & \vdots \\ h_{1n} & \cdots & h_{5n} \end{vmatrix} \begin{vmatrix} \Delta y_{F1} \\ \Delta z_{F1} \\ \Delta y_{F2} \\ \Delta z_{F2} \\ \Delta a \end{vmatrix} = - \begin{vmatrix} e_1 \\ \vdots \\ e_n \end{vmatrix}, \tag{21}$$

where h_{1j} is the function value of the partial derivative $\frac{\partial E}{\partial y_{F1}}$ at jth observation value and initial value, and the other h_{ij} denotes the meaning in the same way and e_j is the jth observation error.

In order to reduce the linearization error, a two-step optimization algorithm, i.e., LMS-PSO, is proposed here. First, an approximate solution of Eq. (18) is obtained through solving linearized Eq. (21) based on the LMS. It is reasonable to insist the accurate solution is near this approximation. Second, the initial population of PSO is generated randomly around the result of the LMS. In detail, the LMS result is taken as the median of the initial population and forced as one initial particle, which could guarantee that the final optimization result must be better than the LMS result. In addition, a mutation link is introduced into the optimization process while the difference between the value of a particle and the median exceeds the threshold. After the coordinates of the two focuses are calculated, the angle between the vector $\overrightarrow{F_2F_1}$ and the axis o_Cy_C is taken as the Euler angle θ_{FC}. The whole simulation process is shown in Fig. 7.

Table 2. Simulation Parameters of θ_{FC}

Parameters		Value
True value	Coordinate of focus (pixel)	(180000,0), (−180000,0)
	a (pixel)	3500
	θ_{FC} (°)	0.008
Noise	Sampling noise of pixel (pixel)	(0.212,0.229,0.364,0.541)[a]

[a]From [33].

Table 3. Calibration Accuracy of Different Sampling Noise

Sampling noise (pixel)	0.212	0.229	0.364	0.541
RMS of error (°)	0.0012	0.0014	0.0021	0.0029

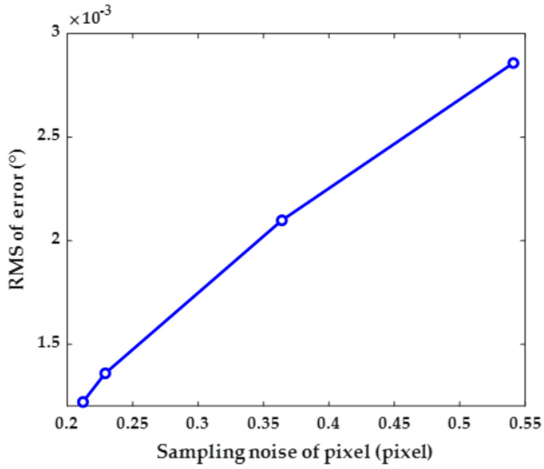

Fig. 8. Variation curve of calibration accuracy with different sampling noise.

According to Fig. 7, the simulation parameters are listed in Table 2.

The above simulation is repeated 100 times for each sampling noise value of pixel. The variation curve of simulated calibration accuracy, i.e., the root mean square (RMS) of error with sampling noise of pixel, is shown in Table 3 and Fig. 8.

It can be seen from Table 3 and Fig. 8 that the simulated RMS of error is positively correlated with the sampling noise of pixel. Accord to [33], the main influence on the sampling noise of pixel is environment vibration, i.e., the coordinate of the image point varies with the random environment vibration. In addition, [33] points out this influence will induce less than 0.5 pixel with single captured image on the vibration isolation foundation usually. According to the error theory in [34], the best way to eliminate random errors is to repeat sampling. When resampling a pixel 25 times, the synthetic sampling noise is 0.229 pixel while the contribution of environment vibration is 0.1 pixel. And when the times of the resampling increase to 100 times, the noise is 0.212 pixel with 0.05 pixel caused by vibration. According to the curve shown in Fig. 8, when the sampling noise is 0.229, the simulated RMS of error is 0.0014° while the simulated RMS of error slightly descends to 0.0012°

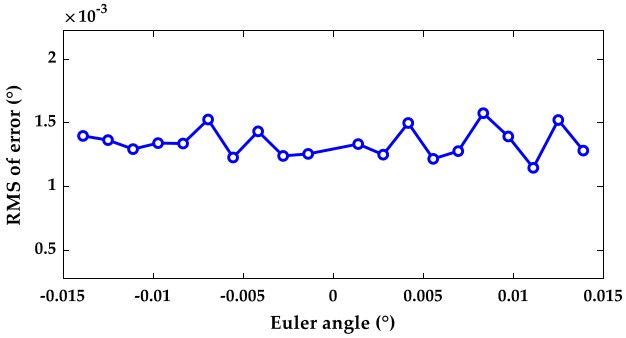

Fig. 9. Fluctuate curve of calibration accuracy with different θ_{FC}.

when its sampling noise is 0.212. On the other hand, when the sampling noise is 0.364 pixel with 0.25 pixel caused by vibration, i.e., resampling a pixel 4 times, the simulated RMS of error will ascend to about 0.0021° urgently. As a result, the noise value 0.229 pixel with 0.1 pixel vibration induced component (i.e., resampling a pixel 25 times) is taken as a balance between the accuracy and workload.

In addition, in order to show the stability of calibration accuracy of different θ_{FC}, the calibration accuracy of different values is also simulated in the interval, i.e., $[-0.014°, 0.014°]$ where θ_{FC} may probably exist, and the result is shown in Table 4 and Fig. 9.

As can be seen from Table 4 and Fig. 9, the range of simulated calibration accuracy is $[0.0011°, 0.0016°]$ of which the mean is 0.0013° and the standard deviation is 0.0001°. It can be concluded that the calibration accuracy is stable no matter what the value of θ_{FC} is and the calibrated accuracy of this method is 0.0047° (3σ). The simulation result at typical value, i.e., $\theta_{FC} = 0.008°$, is shown in Fig. 10.

In Fig. 10, the red dashed line denotes the original hyperbola, the red dashed–dotted line denotes the hyperbola after rotation 0.008°, the red solid line with black diamond denotes the sampling pixel data from the red dashed–dotted line, the black dotted line denotes the simulation result by LMS, while the black solid line denotes the simulation result by LMS-PSO. It could be found obviously that the result of LMS-PSO is closer to the true value compared to the result of LMS.

4. EXPERIMENT AND RESULTS

A. Experiment Setting

In order to verify the validation and actual calibration accuracy of the proposed method, a real-world experiment is conducted. Based on the method proposed in this paper, the calibration work between the FCS and the CCS is divided into two steps. The specific calibration experiment architectures are shown in

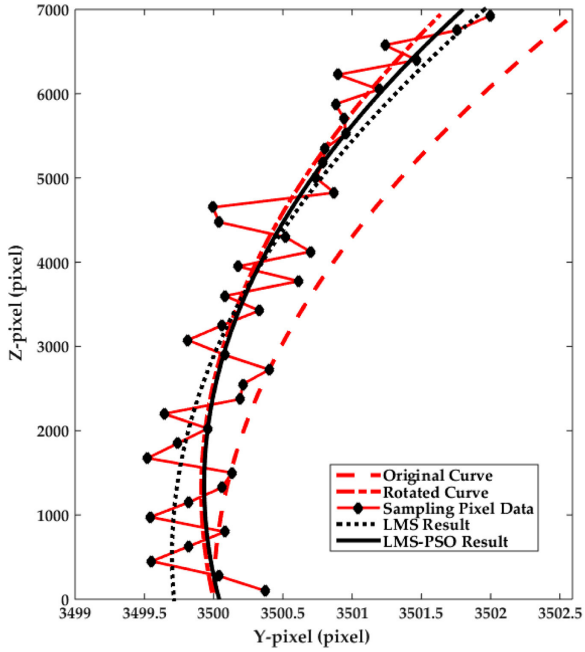

Fig. 10. Simulation result of typical value $\theta_{FC} = 0.008°$.

Table 5. Main Parameters of the Experiment Devices

Device	Manufacture	Model	Main Parameters
Collimator	CIOMP	10 m	Focal length: 10067 mm
Airborne camera	CIOMP	EO-08	Focal length: 1815 mm
Detector	GPIXEL, China	GMAX0603	Number of active pixels: 7542 × 5144
Electric encoder	Netzer	DS-90-64-35H-S0	Bit: 19 Static error: < 0.01°

Fig. 11, while the main parameters of the experiment devices are given in Table 5.

The experiment steps are designed as follows. In the first step, the relationship between the roll axis and the CCS is calibrated. First, the scan head of the airborne camera is taken off. Second, the airborne camera without the scan head is placed in front of the collimator, as is shown in Fig. 11(a). Third, the relative position of the camera with the collimator is adjusted. (Both the camera and the collimator are located on the isolation foundation.) As a result, when the camera rotates around its roll axis with one circle, the image point which passes the collimator could be imaged by the camera. Then the encoder reader and image acquisition computer are connected with the camera respectively. The encoder output value of the roll axis and the

Table 4. Calibration Accuracy of Different θ_{FC}

θ_{FC} (°)	−0.0139	−0.0125	−0.0111	−0.0097	−0.0083	−0.0069	−0.0056
RMS of error (°)	0.0014	0.0014	0.0013	0.0013	0.0013	0.0015	0.0012
θ_{FC} (°)	−0.0042	−0.0028	−0.0014	0.0014	0.0028	0.0042	0.0056
RMS of error (°)	0.0014	0.0012	0.0013	0.0013	0.0013	0.0015	0.0012
θ_{FC} (°)	0.0069	0.0083	0.0097	0.0111	0.0125	0.0139	
RMS of error (°)	0.0013	0.0016	0.0014	0.0011	0.0015	0.0013	

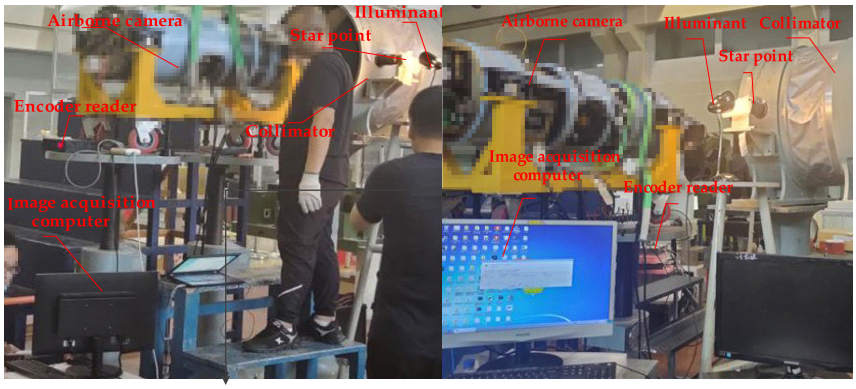

Fig. 11. Experiment architectures: (a) calibration of the roll axis and CCS; (b) calibration of the pitch axis and CCS.

corresponded star point image are recorded at 60 different roll angles of one circle which are approximately equidistant intervals. The image is resampled three times at the same roll angle to obtain the average of the image point coordinate in order to decline the impact of random error. Finally, the acquisition data is disposed to calculate the Euler angle (α_{FC}, β_{FC}). The above process is repeated 10 times to calculate the calibration accuracy. In the second step, the relationship between the pitch axis and the CCS is calibrated. First, the scan head is mounted back on the camera. Second, the camera is placed in front of the collimator, as shown in Fig. 11(b). Third, the relative position of the camera with the collimator is adjusted to image the star point by the camera when the scan mirror sways around its pitch axis. Then the encoder reader and image acquisition computer are connected with the camera respectively. The encoder output value of the pitch axis and the corresponded star point image are recorded at 40 different positions which evenly divide the longitudinal direction (i.e., 7542 pixels) of the detector. The image is resampled 25 times at the same pitch angle to obtain the average of the image point coordinate. Finally, the acquisition data is disposed to calculate the Euler angle θ_{FC}. The above process is repeated 10 times to calculate the calibration accuracy.

B. Experiment Result and Discussion

The calibration experiment of the roll axis and the pitch axis is conducted 10 times respectively. During the experiment, the acquired star image is shown in Fig. 12. The image point coordinates on each image are extracted based on the pixel interpolation subdivision technology [35]. In detail, it takes advantage of the biorthogonal adaptive wavelet algorithm to determine an image gray threshold first which can distinguish the point target from the background accurately. Then the image coordinates are calculated by solving the centroid of the weighted point target. The calibration results are listed in Table 6. As can be seen from Table 6, the calibration uncertainty of the angle coordinate (α_{FC}, β_{FC}) is (0.0025°,0.0015°), and the calibration uncertainty of the angle coordinate (α_0, β_0) is (0.0014°,0.0017°), which are obviously greater than the simulation results. While the calibration uncertainty of the Euler angle θ_{FC} is 0.0037°, which is relatively consistent with the simulation results.

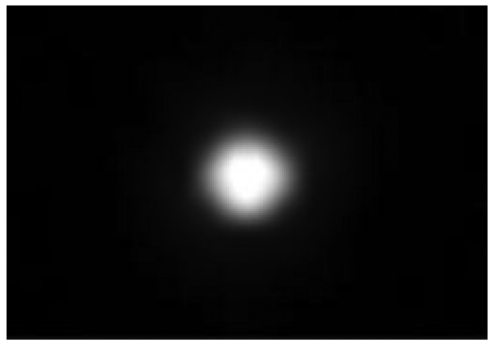

Fig. 12. Star image of the calibration experiment.

Table 6. Calibration Results of Experiment

Parameter No.	α_0 (°)	β_0 (°)	α_{FC} (°)	β_{FC} (°)	θ_{FC} (°)
1	0.0946	0.0720	0.0147	0.0104	0.0047
2	0.0948	0.0725	0.0155	0.0108	0.0015
3	0.0954	0.0719	0.0165	0.0109	0.0041
4	0.0953	0.0720	0.0162	0.0111	0.0062
5	0.0946	0.0723	0.0164	0.0101	0.0040
6	0.0948	0.0732	0.0152	0.0098	0.0055
7	0.0946	0.0721	0.0147	0.0098	0.0042
8	0.0950	0.0730	0.0149	0.0109	0.0048
9	0.0957	0.0723	0.0151	0.0105	0.0039
10	0.0957	0.0733	0.0167	0.0107	0.0040
Error (3σ)	0.0013	0.0016	0.0024	0.0014	0.0037

Fig. 13. Different ground targets of the flight experiment.

Table 7. Geo-Location Error of Flight Experiment

No.	Target Geographic Position[a]	Geo-Location Error (m)		No.	Target Geographic Position[a]	Geo-Location Error (m)	
		Uncalibrated	Calibrated			Uncalibrated	Calibrated
1	(34°25′42.4″N, 113°0′54.2″E)	430.8	142.6	21	(34°21′19.6″N, 113°6′30.5″E)	383.0	47
2	(34°25′42.4″N, 113°1′53.1″E)	245.1	49.4	22	(34°22′01.6″N, 113°6′30.5″E)	483.7	62.1
3	(34°25′42.4″N, 113°2′52.0″E)	351.9	63.7	23	(34°22′43.7″N, 113°6′30.5″E)	229.6	101.7
4	(34°25′42.4″N, 113°3′51.0″E)	368.6	39.1	24	(34°23′25.7″N, 113°6′30.5″E)	251.6	26.4
5	(34°25′42.4″N, 113°4′49.9″E)	253.3	52.1	25	(34°24′07.7″N, 113°6′30.5″E)	334.8	100.8
6	(34°25′42.4″N, 113°5′48.8″E)	395.2	36.8	26	(34°24′49.8″N, 113°6′30.5″E)	249.8	50.6
7	(34°25′42.4″N, 113°6′47.7″E)	149.7	57.4	27	(34°25′31.8″N, 113°6′30.5″E)	213.2	80.3
8	(34°25′42.4″N, 113°7′46.7″E)	361.6	61.2	28	(34°26′13.8″N, 113°6′30.5″E)	514.2	116.1
9	(34°25′42.4″N, 113°8′45.6″E)	647.1	125.9	29	(34°26′55.9″N, 113°6′30.5″E)	523.4	136.8
10	(34°25′42.4″N, 113°9′44.5″E)	472.3	51.8	30	(34°27′37.9″N, 113°6′30.5″E)	321.5	66.7
11	(34°24′58.0″N, 113°0′54.2″E)	373.7	79.4	31	(34°01′19.4″N, 113°7′23.5″E)	435.4	86.5
12	(34°24′58.0″N, 113°1′53.0″E)	306.6	55.4	32	(34°02′01.4″N, 113°7′23.5″E)	167.9	40.3
13	(34°24′58.0″N, 113°2′51.8″E)	399.5	85.3	33	(34°02′43.4″N, 113°7′23.5″E)	179.1	53.7
14	(34°24′58.0″N, 113°3′50.6″E)	280.4	94.8	34	(34°03′25.4″N, 113°7′23.5″E)	513.6	43.2
15	(34°24′58.0″N, 113°4′49.4″E)	156.4	116.8	35	(34°04′07.4″N, 113°7′23.5″E)	259.9	61.9
16	(34°24′58.0″N, 113°5′48.1″E)	561.8	127.8	36	(34°04′49.5″N, 113°7′23.5″E)	539.3	131.6
17	(34°24′58.0″N, 113°6′46.9″E)	409.4	58.4	37	(34°05′31.5″N, 113°7′23.5″E)	370.1	98.3
18	(34°24′58.0″N, 113°7′45.7″E)	398.4	132.7	38	(34°06′13.5″N, 113°7′23.5″E)	291.1	72.7
19	(34°24′58.0″N, 113°8′44.5″E)	312.1	99.2	39	(34°06′55.5″N, 113°7′23.5″E)	301.9	27.5
20	(34°24′58.0″N, 113°9′43.3″E)	370.5	78.2	40	(34°07′37.5″N, 113°7′23.5″E)	343.2	59.9
Uncalibrated RMS of Geo-location error (m)			372.6	Calibrated RMS of Geo-location error (m)			83.3

[a]Altitude of the ground targets: 2002 m.

After the ground calibration experiment, an actual flight experiment is also conducted to fully illustrate the effect on the improvement of the target geo-location accuracy. The camera is mounted on a certain type of aircraft to image the 40 targets laid on the ground. The ground targets are shown in Fig. 13. First, the geographic positions of these ground targets are measured through a GPS device and treated as the true values. Second, the geographic positions of the targets are directly calculated based on the image and its remark information by Qiao's method [3]. Then, the calibrated parameters in this paper are introduced into the solving process of Qiao's method [3] to calculate the geographic positions of the targets. The two calculation values are compared with the true values and the statistical error result is shown in Table 7.

It can be seen from Table 7 that the target geo-location accuracy of the airborne camera without extrinsic parameters calibration is 372.6 m while the target geo-location accuracy with extrinsic parameters calibration is 83.3 m. It can be concluded that the method in this paper is effective and feasible, and the final target geo-location accuracy can meet the customer's requirements. In addition, in order to further illustrate the superiority of our improved algorithms, a comparative experiment with the matured algorithms, i.e., LMS and PSO-GA, in current state-of-the-arts has been conducted. Specifically, the original experimental data of the extrinsic parameters calibration are

Table 8. Geo-Location Error Compared with State-of-the-Art

Algorithm	Geo-Location Error (m)	Comparative Result (m)
LMS	137.1	−53.8
PSO-GA	109.2	−25.9
Improve algorithm of this paper	83.3	–

used to calibrate the extrinsic parameters again by the LMS and PSO-GA, respectively. Then the calibrated results combined with the flight experiment images are used to calculate the geographic positions of the ground targets through Qiao's method [3]. The target geo-location accuracy is shown in Table 8.

It can be seen from Table 8 that the target geo-location accuracy with our improved algorithms is 53.8 m higher than the accuracy with the LMS, while the target geo-location accuracy with our improved algorithms is 25.9 m higher than the accuracy with the PSO-GA. Therefore, in view of this problem, it can be concluded that the improved algorithms in this paper have advantages over the matured algorithms LMS and PSO-GA, under the same condition.

In view of the calibration problem in this paper and the above experiment results, the existing problems and the prospect of future work are discussed as follows:

1. There are differences between the experiment results and simulation results of the roll axis calibration. It may be explained by the following reasons. When the camera rotates around its roll shaft system, the roll axis is wobbling rather than a fixed vector in space. The second possible reason is that there are various errors in the angle encoder and its reader which could result in the deviations of the dynamic variable. Another possible reason is that the sampling error of image points is large due to the large foundation vibration during image acquisition.
2. The experiment results of the pitch axis are relatively consistent with the simulation results. Although the pitch shaft system also has the problem of wobbling, the influence of shaft wobbling can be almost ignored because the angle of view of the optical system is small and it can be covered when the scanning mirror sways a small angle near 45°.
3. There is a slight principle error in the calibration of θ_{FC}, i.e., when θ_{FC} is being calibrated; it is considered that the angle coordinate of the roll axis $(\alpha_{FC}, \beta_{FC})$ is very small and about equal to 0, so its influence on the calibration can be ignored on which the subsequent derivation is based. In addition, the LMS-PSO method used in this paper can effectively reduce the principle error caused by linearization of non-linear equations and find a better solution than the LMS method.
4. From the result of the actual flight experiment, it can be seen that the target geo-location accuracy has been remarkably improved from 372.6 to 83.3 after using the calibrated parameters in this paper. This might not be only attributed to the extrinsic parameters calibration, but also the intrinsic parameters calibration is helpful to increase the accuracy. However, by comparing with current state-of-the-arts, the method proposed in this paper does have its advantages.
5. In the future, we can focus on the influence of shaft wobbling on the extrinsic parameters of the camera and the influence of orthogonality between the roll axis and the pitch axis on the target geo-location accuracy. In addition, as mentioned above, the calibration method for the pitch axis can establish more rigorous mathematical model to eliminate the existing principle errors. We can also verify the effect of the work of this paper on the improvement of target geo-location accuracy through the actual flight experiment.
6. The two-step calibration method is not limited to the algorithms proposed in this paper. In addition, the method proposed in this paper can simultaneously calibrate the intrinsic parameters of the airborne camera.

5. CONCLUSION

This paper proposes a calibration method for the extrinsic parameters of an airborne camera, i.e., the orientation relationship between the FCS and the CCS. The calibration mathematical principle is given, and its numerical simulation is carried out. Finally, the effectiveness of the proposed method is verified through a real-world experiment. And the experiment results show that the calibration accuracy of each Euler angle can reach 0.0037° (3σ).

Funding. National Major Science and Technology Projects of China (30-H32A01-9005-13/15).

Acknowledgment. The system calibration is performed at the Key Laboratory of Airborne Optical Imaging and Measurement at Changchun Institute of Optics, Fine Mechanics and Physics, Chinese Academy of Sciences. It is gratefully acknowledged. And D.Y. would also like to deeply thank his supervisor for the advice and his colleagues for their cooperation on the experiments.

Disclosures. The authors declare no conflicts of interest.

REFERENCES

1. C. S. Sun, Y. L. Ding, D. J. Wang, and D. P. Tian, "Backscanning step and stare imaging system with high frame rate and wide coverage," Appl. Opt. **54**, 4960–4965 (2015).
2. M. Pachter, N. Ceccarelli, and P. R. Chandler, "Vision-based target geolocation using micro air vehicles," J. Guid. Control Dyn. **31**, 597–615 (2008).
3. C. Qiao, Y. L. Ding, Y. S. Xu, and J. H. Xiu, "Ground target geolocation based on digital elevation model for airborne wide-area reconnaissance system," J. Appl. Remote Sens. **12**, 1 (2018).
4. S. Hui, "Target localization and error analysis of airborne electro-optical platform," Chin. J. Opt. Appl. Opt. **6**, 912–918 (2013).
5. J. Li and Z. Liu, "Camera geometric calibration using dynamic single-pixel illumination with deep learning networks," IEEE Trans. Circuits Syst. Video Technol. **30**, 2550–2558 (2020).
6. M. Arbabmir and M. Ebrahimi, "Visual–inertial state estimation with camera and camera–IMU calibration," Rob. Auton. Syst. **120**, 103249 (2019).
7. R. Azuma and G. Bishop, "Improving static and dynamic registration in an optical see-through HMD," in *Proceedings of the 21st Annual Conference on Computer Graphics and Interactive Techniques, SIGGRAPH* (1994).
8. M. Bajura and U. Neumann, "Dynamic registration correction in video-based augmented reality systems," IEEE Comput. Graph. Appl. **15**, 52–60 (1995).
9. P. Sturm, "Pinhole camera model," in *Computer Vision: A Reference Guide*, K. Ikeuchi, ed. (Springer, 2014), pp. 610–613.

10. S. M. Paniit and W. Zhang, "Modeling random gyro drift rate by data dependent systems," IEEE Trans. Aerosp. Electron. Syst. **22**, 455–460 (1986).
11. Y. Wu, J. Wang, X. Wang, and M. Alqurashi, "Stochastic modelling and estimation of inertial sensors," Lect. Notes Electr. Eng. **305**, 499–510 (2014).
12. S. You, U. Neumann, and R. Azuma, "Hybrid inertial and vision tracking for augmented reality registration," in *IEEE Virtual Reality* (1999).
13. J. Lobo and J. Dias, "Vision and inertial sensor cooperation using gravity as a vertical reference," IEEE Trans. Pattern Anal. Mach. Intell. **25**, 1597–1608 (2013).
14. J. Lobo and J. Dias, "Inertial sensed ego-motion for 3D vision," J. Robot. Syst. **21**, 3–12 (2010).
15. B. K. P. Horn, H. M. Hilden, and S. Negahdaripour, "Closed-form solution of absolute orientation using orthonormal matrices," J. Opt. Soc. Am. A **5**, 1127–1135 (1988).
16. L. Wang and H. H. Ju, "Extrinsic calibration of a fisheye camera and inertial measurement unit," in *International Conference on Machine Learning & Cybernetics* (2009).
17. J. D. Hol, T. B. Schoen, and F. Gustafsson, "Modeling and calibration of inertial and vision sensors," Int. J. Robot. Res. **29**, 231–244 (2010).
18. C. Ouyang, S. Shi, Z. You, and K. Zhao, "Extrinsic parameter calibration method for a visual/inertial integrated system with a predefined mechanical interface," Sensors **19**, 3086 (2019).
19. D. Xu, H. W. Wang, Y. F. Li, and M. Tan, "A new calibration method for an inertial and visual sensing system," Int. J. Autom. Comput. **09**, 299–305 (2012).
20. G. Pandey, J. Mcbride, S. Savarese, and R. Eustice, "Extrinsic calibration of a 3D laser scanner and an omnidirectional camera," IFAC Proc. Vol. **43**, 336–341 (2010).
21. H. Aliakbarpour, P. Nuez, J. Prado, K. Khoshhal, and J. Dias, "An efficient algorithm for extrinsic calibration between a 3D laser range finder and a stereo camera for surveillance," in *International Conference on Advanced Robotics* (2009).
22. Y. Fang, C. Cappelle, and Y. Ruichek, *Extrinsic Calibration between 2D Laser Range Finder and Fisheye Camera* (Springer International Publishing, 2014), pp. 925–935.
23. W. Dong and V. Isler, "A novel method for the extrinsic calibration of a 2-D laser-rangefinder & a camera," in *IEEE International Conference on Robotics & Automation* (2017).
24. L. Yin, X. Wang, Y. Ni, K. Zhou, and J. Zhang, "Extrinsic parameters calibration method of cameras with non-overlapping fields of view in airborne remote sensing," Remote Sens. **10**, 1298 (2018).
25. L. Deng, G. Lu, Y. Shao, M. Fei, and H. Hu, "A novel camera calibration technique based on differential evolution particle swarm optimization algorithm," Neurocomputing **174**, 456–465 (2016).
26. K. J. Held and B. H. Robinson, "TIER II Plus airborne EO sensor LOS control and image geolocation," in *IEEE Aerospace Conference* (1997), Vol. **2**, pp. 377–405.
27. C. Qiao, Y. L. Ding, Y. S. Xu, J. H. Xiu, and Y. L. Du, "Ground target geo-location using imaging aerial camera with large inclined angles," Opt. Precis. Eng. **25**, 1714–1726 (2017).
28. Z. Zhang, "A flexible new technique for camera calibration," IEEE Trans. Pattern Anal. Mach. Intell. **22**, 1330–1334 (2000).
29. G. Yuan, L. Zheng, J. Sun, X. Liu, X. Wang, and Z. Zhang, "Practical calibration method for aerial mapping camera based on multiple pinhole collimator," IEEE Access **8**, 39725–39733 (2020).
30. J. Zhang, Y. Ding, L. Zhang, H. Tian, and G. Yuan, "Precise alignment method of time-delayed integration charge-coupled device charge shifting direction in aerial panoramic camera," Opt. Eng. **55**, 125101 (2016).
31. K. Schwertz and J. H. Burge, *Field Guide to Optomechanical Design and Analysis* (SPIE, 2012), pp. 1–30.
32. S. Bi, D. Yang, and Y. Cai, "Automatic calibration of odometry and robot extrinsic parameters using multi-composite-targets for a differential-drive robot with a camera," Sensors **18**, 3097 (2018).
33. J. Zhang, "Research on calibration method of TDI direction for focal plane assembly in aerial panoramic camera," Doctoral dissertation (University of the Chinese Academy of Sciences, 2018).
34. Y. Mao, "Stochastic error," in *Error Theory and Accuracy Analysis* (Defense Industry, 1982), pp. 20–46.
35. G. Z. Li, J. G. Liu, and Z. H. Hao, "Research of subpixel subdivision location algorithm for star image based on biorthogonal wavelet," Opt. Precis. Eng. **13**, 217–221 (2005).